Journal of *Marine Science and Engineering*

MDPI

Article

Numerical Comparison of Piston-, Flap-, and Double-Flap-Type Wave Makers in a Numerical Wave Tank

Kaicheng Yan [1], Haoyu Dou [2], Jungkeun Oh [2] and Daewon Seo [2,*]

[1] School of Marine Engineering Equipment, Zhejinag Ocean University, Zhoushan 316000, China
[2] Department of Naval Architecture and Ocean Engineering, Kunsan National University, Gunsan 54150, Republic of Korea
* Correspondence: dwseo@kunsan.ac.kr; Tel.: +82-63-469-1858

Abstract

In naval and ocean engineering, accurate simulation of incident waves is essential for predicting the motion response of offshore structures. Traditional wave generation methods, such as piston- and flap-type wave makers, often face challenges in accurately replicating the orbital motion of water particles beneath the free surface, which can limit their applicability in high-fidelity simulations. In this study, a numerical investigation is conducted to compare the performance of piston-type, flap-type, and double-flap-type wave makers using STAR-CCM+2310(18.06.006-R8). The influence of water depth on wave height accuracy is evaluated across different measurement locations within a numerical wave tank. Theoretical analysis of wave generation mechanisms is incorporated to clarify the applicability limits of linear theory and to better interpret the numerical results. Results indicate that, under the tested two-dimensional CFD conditions, the double-flap-type wave maker tended to provide closer agreement with theoretical predictions, particularly at greater depths, compared with conventional methods. These findings suggest potential advantages of the double-flap configuration and provide insights for refining wave generation techniques in numerical and experimental wave tanks, thereby supporting more reliable hydrodynamic analyses of floating structures.

Keywords: piston-type wave maker; flap-type wave maker; dual-flap wave-making method; numerical wave tank; wave theory; computational fluid dynamics (CFD)

check for updates

Academic Editor: Mariano Buccino

Received: 16 September 2025
Revised: 22 November 2025
Accepted: 24 November 2025
Published: 28 November 2025

Citation: Yan, K.; Dou, H.; Oh, J.; Seo, D. Numerical Comparison of Piston-, Flap-, and Double-Flap-Type Wave Makers in a Numerical Wave Tank. *J. Mar. Sci. Eng.* **2025**, *13*, 2273. https://doi.org/10.3390/jmse13122273

Copyright: © 2025 by the authors. Licensee MDPI, Basel, Switzerland. This article is an open access article distributed under the terms and conditions of the Creative Commons Attribution (CC BY) license (https://creativecommons.org/licenses/by/4.0/).

1. Introduction

Researchers in naval and ocean engineering have continuously advanced wave-making technologies to accurately reproduce real ocean waves, enabling precise model tests for hydrodynamic studies. A high-performance wavemaker is essential for generating realistic sea states and ensuring reliable measurements of floating body motion responses.

Beyond the development of specific mechanical configurations, a solid theoretical foundation is crucial for understanding the applicability and limitations of different wave generation methods. Dean and Dalrymple [1] established the classical linear wave generation theory, which relates paddle motion to the resulting wave characteristics and remains fundamental to the design of both piston- and flap-type wavemakers. Furthermore, the quality of wave generation in experimental and numerical tanks has been critically assessed in previous studies. Blenkinsopp and Chaplin [2] emphasized the importance of wave propagation distance, boundary reflections, and gauge placement in accurately evaluating wave quality, highlighting that measurement location significantly affects wave field interpretation and validation.

Traditionally, piston-type and flap-type wavemakers have been widely used. The piston type generates waves through the translational motion of a vertical paddle, whereas the flap type relies on rotational motion about a hinge. However, these conventional methods are primarily based on first-order linear wave theory and do not fully capture the disturbances induced by paddle actuation, which can limit their accuracy in certain conditions. To improve wave generation performance, researchers have proposed various enhancements and alternatives. For example, Kim et al. [3] introduced a multifunctional wavemaker combining piston and flap motions, while Kwon et al. [4] and Oh et al. [5] validated piston-type wave makers under different parametric conditions using potential flow and viscous flow solvers. Other studies explored novel mechanisms, such as slider-crank devices for adjustable amplitude [6], nonlinear effects in flap-type operation [7], and numerical wave tanks with flap-type generators to reproduce both regular and irregular waves [8,9]. Further refinements include improved flap-type wave generation equations [10], linear theories for single- and double-flap configurations [11], and advanced numerical schemes such as SPH [12].

Fabio M. and Marques Machado [13] conducted a comparative study on wave generation using different boundary velocity methods and piston-type wave makers. The results indicated that the boundary velocity method is more significantly affected by wave damping, whereas the piston-type wavemaker can generate waves with higher accuracy. Folley et al. [14] employed a combination of experimental and numerical approaches to investigate the effects of varying water depths and wave heights on wave energy capture. Their findings revealed that shallower water depths and higher wave heights generally lead to greater wave energy extraction. Tian et al. [15] constructed a numerical wave tank to investigate the interaction between cylindrical structures and waves. The velocity inlet method was employed for numerical wave generation, while wave absorption was achieved through damping zones at the outlet. The study successfully generated regular waves with high accuracy and maintained stable wave propagation over a period of time. In addition, particle-based numerical wave tanks have been employed for device-scale analyses, demonstrating the practicality of numerical wave generation frameworks in engineering applications [16], and the influence of wave-generation distance on predicted responses has been quantitatively examined, motivating careful placement of gauges and downstream damping arrangements [17]. Numerical and experimental validations have also advanced the field: OpenFOAM-based simulations of OWSCs in extreme seas [18], centrifuge-compatible wave tanks [19], hybrid piston–flap–swing systems [20], irregular wave reproduction in laboratories [21], and piston-type theories for solitary and cnoidal waves [22]. Collectively, these efforts highlight significant progress in wavemaker design and application. Despite these advances, important research gaps remain. Most prior works focus on piston-type or flap-type wave makers separately, without direct comparisons under identical conditions. Studies on dual-flap wave makers are limited, particularly regarding their accuracy at different water depths. Kim [23] eliminated wave reflection by adjusting the mesh size in the damping zone to achieve numerical attenuation, and determined the optimal computational configuration through variations in grid resolution. Hyun [24] developed a theoretical model for an articulated double-flap wavemaker in constant water depth based on Biesel's linear theory. The study analyzed the hydrodynamic characteristics of the upper and lower flaps using a two-dimensional irrotational flow framework. Results showed that, under short-wave conditions ($\lambda/h < 1$), the double-flap configuration effectively reduces inertia pressure and waveform distortion, while appropriate adjustment of the angle and length ratios improves the wave amplitude-to-stroke efficiency (a/S). For long-wave conditions, however, the single-flap or piston-type wavemakers exhibited better performance. This work laid an important foundation for

subsequent studies on multi-flap and CFD-based wave generation theories. Kusumawinahyu et al. [25] developed a linear theory for single- and double-flap wavemakers based on Biesel and Hyun's work. Assuming two-dimensional incompressible and irrotational flow, they derived analytical relations between wave amplitude (H) and flap stroke (S). Results show that the single flap performs better for long waves, while the double flap, with frequency-split motion of the upper and lower flaps, can efficiently generate regular waves over a wider frequency range. A Figure of Merit (FoM) was proposed to evaluate wavemaker efficiency. Proper hinge depth and angle ratio design reduce waveform distortion and energy loss, forming a key theoretical basis for multi-flap and CFD-based wave generation models. Moreover, although numerical and experimental validations exist for individual mechanisms, systematic evaluations of their relative efficiency, wave height accuracy, and dissipation during propagation remain scarce.

To address these gaps, this study following the theoretical approaches discussed by Madsen, O. [26], Issa, R. I. [27], and Ferziger, J. H. et al. [28] numerically investigates piston-type, flap-type, and double-flap-type wavemakers under varying water depths using STAR-CCM+. Wave heights are compared with theoretical predictions at multiple measurement locations, and the influence of water depth on wave generation accuracy is quantified. The results provide new insights into the potential advantages of the double-flap configuration over conventional designs, contributing to the optimization of wave-making technologies for ocean engineering applications.

2. Numerical Methodology

2.1. Governing Equations

In general, the fluid in naval and ocean engineering applications is assumed to be viscous and incompressible. The governing equations for the flow field consist of the continuity equation (Equation (1)), the Navier–Stokes equations (Equation (2)), and the turbulence equations.

$$\frac{\partial \rho}{\partial t} + \frac{\partial (\rho u_i)}{\partial x_i} = 0 \tag{1}$$

$$\frac{\partial}{\partial t}(\rho u_i) + \frac{\partial}{\partial x_i}(\rho u_i u_j) = -\frac{\partial p}{\partial x_i} + \frac{\partial}{\partial x_i}[\mu\left(\frac{\partial u_i}{\partial x_j} + \frac{\partial u_i}{\partial x_i}\right) - \rho\overline{u_i' u_j'}] \tag{2}$$

Here, (i = 1, 2, 3) corresponds to the velocity components in the x-, y-, and z-directions within a Cartesian coordinate system. ρ denotes the fluid density, p is the pressure, and g represents the gravitational acceleration vector.

It is noted that Equations (1) and (2) do not form a closed system for incompressible flow.

In the incompressible Navier–Stokes formulation, the pressure does not possess its own governing equation because the continuity equation eliminates the density variation and removes a pressure time-derivative term. As a result, pressure cannot be solved explicitly from Equations (1) and (2). Instead, the pressure field must be obtained implicitly by enforcing mass conservation through a pressure–velocity coupling algorithm (e.g., SIMPLE or PISO). This coupling step ensures that the velocity field satisfies the divergence-free constraint at every time step, thereby closing the system of equations.

All numerical simulations were performed in a two-dimensional numerical wave tank (2D-NWT), consistent with the linear-theory-based evaluation of paddle-generated regular waves. To represent the prescribed paddle motion, an overset mesh was employed around the moving piston/flap region. The overset block is a locally refined rectangular zone that moves rigidly with the wavemaker, while the surrounding background mesh remains stationary. Grid communication between overset and background regions is performed

through the conservative trilinear interpolation scheme provided in STAR-CCM+, ensuring momentum-consistent transfer of velocity and pressure.

A minimum separation of approximately 2–3 cells was maintained between the overset boundary and the background mesh to avoid mesh squeezing during large-amplitude motions. No special near-wall treatments were required because the grid resolution near the moving boundaries was set to maintain $y^+ < 1$, permitting the use of low-Reynolds-number wall treatment compatible with the VOF interface.

The overset configuration eliminates mesh distortion and preserves grid quality throughout the entire stroke of the wavemaker, improving numerical stability during long-duration wave propagation simulations.

2.2. Principles of Wave Generation

2.2.1. Piston-Type Wave Generation

The piston-type wavemaker is one of the most commonly used devices for generating regular waves in both physical and numerical wave tanks. As illustrated in Figure 1, it consists of a vertical plate that oscillates horizontally in a reciprocating motion to produce free-surface waves. The plate extends from the tank bottom to the still-water level (z = 0), with the water depth denoted by h, and the waves propagate in the x-direction. During the forward motion, the plate pushes the adjacent water mass, causing a local rise in the free surface and the formation of a wave crest. Conversely, during the backward motion, the plate retracts, drawing water toward itself and generating a trough. Through the continuous harmonic oscillation of the plate, a series of periodic wave crests and troughs are formed and propagate along the tank, producing stable regular waves.

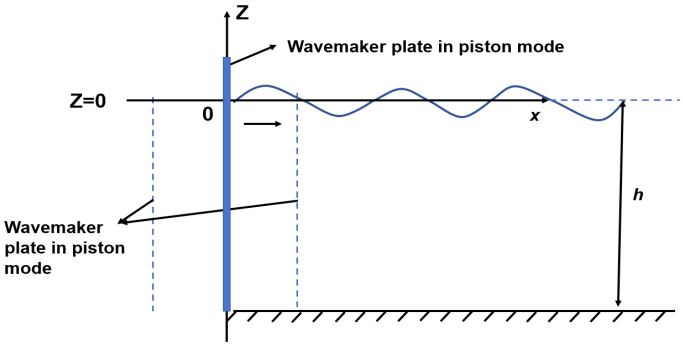


Figure 1. Schematic Diagram of Piston-Type Wavemaker Operation.

The paddle's motion follows the theoretical approximation developed by Madsen [21], as defined in Equations (3) and (4). The stroke length in the x-direction is set to 0.115 m, as given in Equation (5), and the paddle oscillates sinusoidally in time, as described in Equation (6). Under these conditions, the generated linear wave exhibits a height of 0.06 m and a wavelength of 3 m.

$$\sigma = \frac{2\pi}{T} \tag{3}$$

$$m_1 = \frac{4\sin h^2 kh}{\sin h 2kh + 2kh} \tag{4}$$

$$S_0 = \frac{H}{m_1} \tag{5}$$

$$X_0(t) = \frac{H}{2m_1}\sin\sigma t + \frac{H^2}{32h}\left(\frac{2\cos kh}{\sin h^3 kh} - \frac{2}{m_1}\right)\sin\sigma t \tag{6}$$

2.2.2. Flap-Type Wave Generation

The flap-type wavemaker generates surface waves by rotating a vertical plate about a hinge located near the bottom of the tank. The periodic angular motion of the plate induces the oscillation of the free surface, thereby forming propagating waves. By adjusting the rotational amplitude and frequency, the flap-type wavemaker can effectively control the wave characteristics, including height and wavelength. Owing to its simple configuration and ease of installation, this type of wavemaker is particularly suitable for generating waves under deeper water conditions. A schematic diagram of the flap-type wavemaker is presented in Figure 2, where h denotes the water depth and d represents the hinge depth.

$$A = \frac{\sinh(kh)}{2}\frac{\int_{-d}^{0}\frac{1}{2}(1+\frac{z}{d})\cosh k(h+z))dz}{\int_{-h}^{0}\cosh^2(k(h+z))dz}S = 2(\frac{\sinh kh}{kd})\frac{\cosh k(h-d)+\mathrm{kd}\cdot\sinh(kh)-\cosh(kh)}{2kh+\sinh(2kh)}S$$

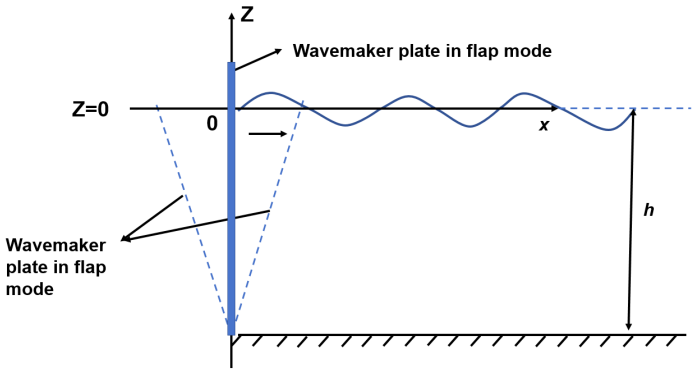


Figure 2. Schematic Diagram of Flap-Type Wavemaker Operation.

2.2.3. Double Flap-Type Wave Generation

The double-flap-type wavemaker generates surface waves through the combined rotational motions of two hinged flaps positioned at different depths along a vertical plate, as illustrated in Figure 3. The lower flap rotates about a hinge located near the tank bottom (Q_1), while the upper flap pivots around an intermediate hinge (Q_2). Depending on the desired wave conditions, the two flaps can operate either independently or synchronously. By adjusting the rotational amplitudes and phase differences between the upper and lower flaps, the double-flap wavemaker effectively controls the wave frequency range—where the upper flap primarily generates short-period waves, and the lower flap produces long-period waves. This dual-motion configuration significantly improves the quality of the generated waves by suppressing higher harmonics and minimizing wave reflections near the wavemaker boundary. In the schematic, h denotes the total water depth, h_1 and h_2 represent the depths of the lower and upper hinges, respectively, and S indicates the instantaneous displacement of the upper flap surface, with waves propagating in the x-direction.

$$H_1 = 4(\frac{\sinh k_1 h}{k_1 d_1})\frac{\cosh k_1(h-d_1)+k_1 d_1 \sinh k_1 h-\cosh k_1 h}{2k_1 h+\sinh 2k_1 h}S_1,$$

$$H_2 = 4\left(\frac{\sinh k_2 h}{k_2 d_2}\right)\frac{\cosh k_2(h-d_2)+k_2 d_2\cdot\sinh(k_2 h)-\cosh k_2 h}{2k_2 h+\sinh 2k_2 h}S_2.$$

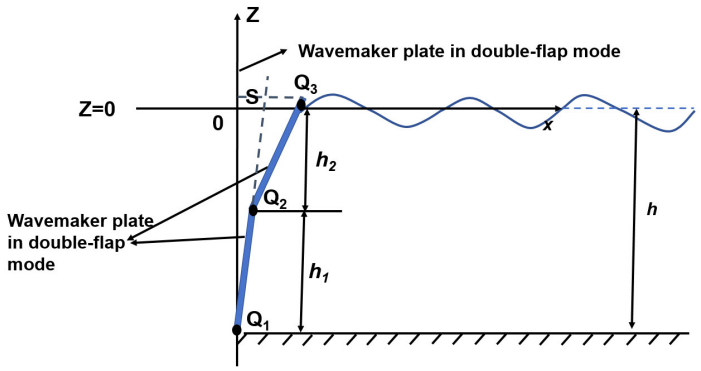


Figure 3. Schematic Diagram of Double Flap-Type Wavemaker Operation.

These relate the wave heights H_1 and H_2 to the strokes S_1 and S_2, respectively.

For $\omega_1 \neq \omega_2$, the maximum wave height is $H_1 + H_2$ and the minimum wave height is $|H_1 - H_2|$ in the generated bi-chromatic wave pattern.

3. Numerical Modeling and Wave Generation Analysis

3.1. Grid Sensitivity Test

Figure 4 presents the overall layout and zoning of the piston-type wavemaker model in a numerical or physical wave tank (The flap-type and double-flap wavemakers are based on the same physical configuration). The wavemaker is installed on the left side of the tank and generates waves in the wave generation zone through periodic rotation about a hinge point. The produced waves propagate rightward through the working zone and are subsequently absorbed in the damping zone to minimize wave reflection. The still-water depth is denoted by h, and the total tank length is represented by L. The region above the free surface corresponds to the air phase, while a wave probe is positioned within the working zone to record the temporal variations in the free-surface elevation.

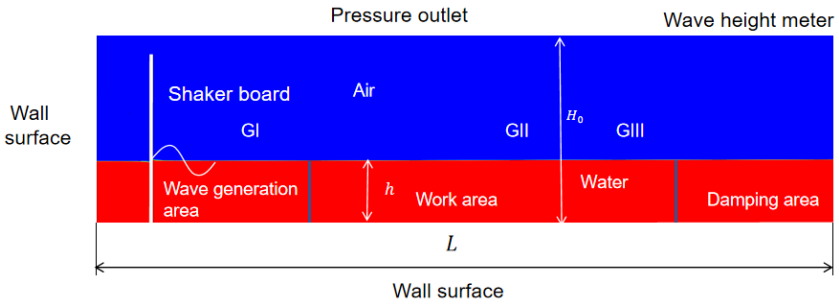


Figure 4. Schematic Diagram of the Numerical Wave Tank (NWT).

Figure 5 illustrates the mesh configuration and zoning of the two-dimensional numerical wave tank. The total tank length is 60 m and the height is 3 m. A uniform mesh with a base cell size of 0.05 m was applied from the wavemaker up to 20 m (mesh addition zone), while the downstream region (20–60 m) employed a gradually coarsening mesh generated using the extruder technique to reduce computational cost while maintaining numerical stability. Near the free surface, the vertical grid was refined to accurately capture surface deformation.

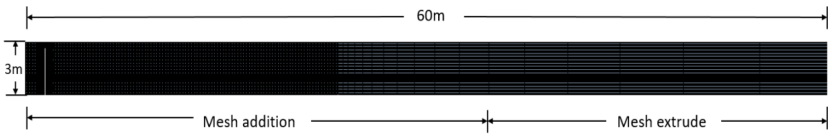


Figure 5. Computational mesh for piston-type wave maker.

In addition to the conventional damping zone placed at the downstream boundary to absorb reflected waves, this study further utilized the extruder-based mesh extension method to achieve smooth cell-size transitions and energy dissipation, thereby effectively minimizing numerical reflection. This approach ensured that the incident waves generated by the wavemaker propagated stably through the working zone without interference from reflected waves. The combined application of the damping zone and extruder technique enabled long-duration simulations with consistent wave propagation and minimal reflection effects, ensuring high numerical accuracy in the evolution of the free surface (All subsequent simulations in this study adopted this configuration).

To analyze the wave height and propagation characteristics of the numerically generated waves, three monitoring probes were placed at distances of 3 m, 5 m, and 8 m downstream from the wavemaker paddle to record the free-surface elevations. The measured time series were then compared with the corresponding theoretical solutions, as illustrated in Figure 5.

The generated waves are based on the approximation proposed by Madsen [26], with a wave period of 2 s and a wave height of 0.06 m, propagating through the numerical wave tank. To investigate the influence of time step size on numerical damping, wave heights are evaluated at a location farther downstream from the wave paddle. To evaluate the influence of grid resolution on simulation accuracy, four mesh configurations were examined, as summarized in Table 1 and Figure 6. In Case G4, a highly refined grid was employed, providing approximately 40 cells per wave height (0.05 m) with a total of about 0.98 million cells. Cases G1, G2, and G3 adopted progressively coarser meshes corresponding to 5, 10, and 20 cells per wave height, resulting in total grid counts of approximately 0.55 million, 0.15 million, and 0.05 million, respectively. This mesh sensitivity analysis was conducted to verify grid convergence of the simulated wave parameters and to achieve an optimal balance between numerical accuracy and computational efficiency.

Table 1. Grid resolution cases for sensitivity analysis.

Case	Cells per Wave Height	Number of Grid Cells (Million)	Grid Level
G1	5	0.05	Very fine
G2	10	0.15	Fine
G3	20	0.55	Medium
G4	40	0.98	Coarse

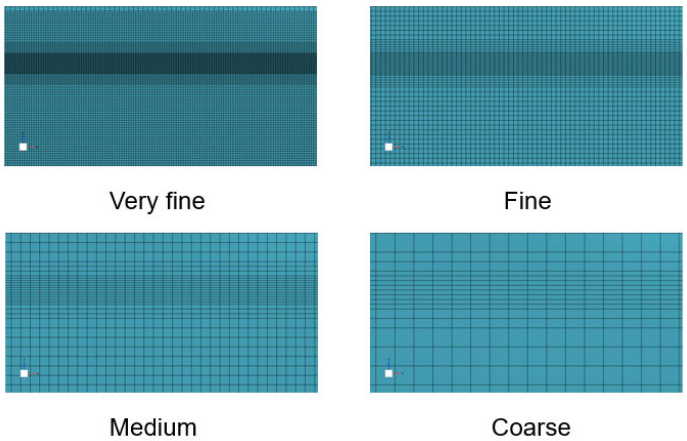


Figure 6. Visualization of mesh resolution levels used in the grid-sensitivity analysis.

The Figures 7–9 below shows the temporal variations in free-surface elevations at three monitoring locations (3 m, 5 m, and 8 m downstream) under different mesh refinement levels (G1–G4).

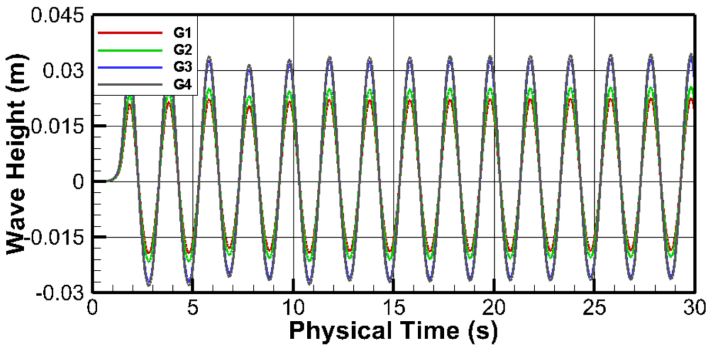


Figure 7. Wave elevation comparison at 3 m downstream (G1–G4).

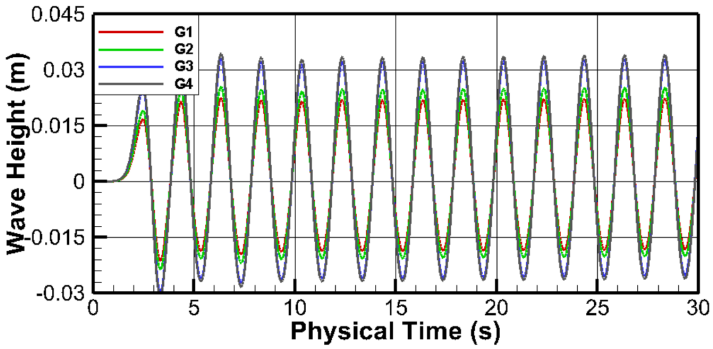


Figure 8. Wave elevation comparison at 5 m downstream (G1–G4).

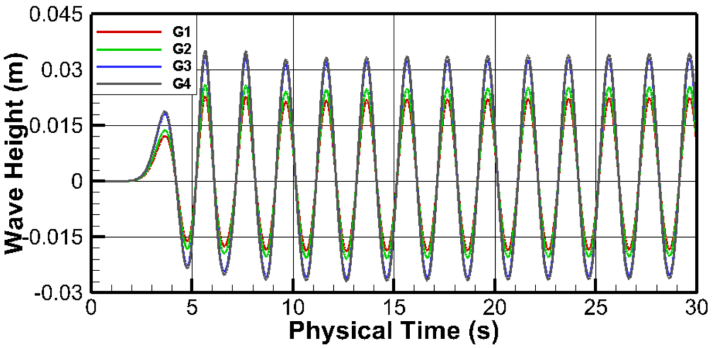


Figure 9. Wave elevation comparison at 8 m downstream (G1–G4).

Figure 10 compares the numerically simulated wave heights with the theoretical results under different grid resolutions. In Cases G1 and G2, where each wave height contains more than 20 cells per wave height, the numerical results show excellent agreement with the theoretical wave profile, maintaining an overall accuracy above 98%, and the accuracy does not significantly improve with further grid refinement. In contrast, Cases G3 and G4, which employ fewer than 10 cells per wave height, exhibit deviations exceeding 10%, indicating that wave height prediction is highly sensitive to vertical grid resolution.

Considering that the total number of cells in Case G1 is nearly twice that of Case G2, and taking into account both computational cost and numerical accuracy, Case G2 (corresponding to 20 cells per wave height) was selected for subsequent simulations as it provides an optimal balance between efficiency and precision.

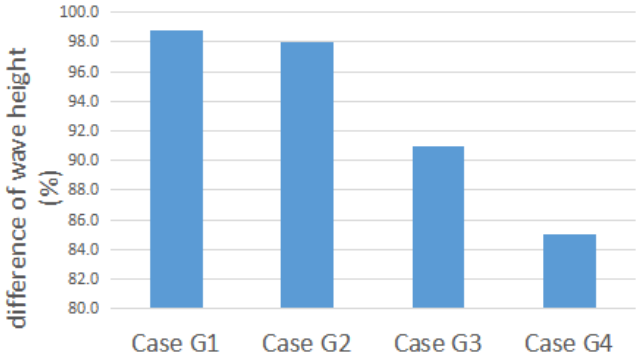


Figure 10. Comparison of numerical and theoretical wave height accuracy under different grid resolutions at x = 8 m.

3.2. Time Step Independence Test

For this analysis, numerical simulations are performed using four different non-dimensional time step sizes (T/Δt), as summarized in Table 2. Throughout the simulations, the spatial grid resolution is held constant at 20 grid points per wave height and 250 grid points per wavelength to ensure consistent spatial accuracy.

Table 2. Time step cases for sensitivity analysis.

Case	Time Steps per Wave Period	Courant Number
T1	400	0.95
T2	600	0.50
T3	800	0.10
T4	1000	0.05

To ensure numerical stability and temporal accuracy, the Courant number (Co) was evaluated for each time-step case. The Courant number is defined as $Co = \frac{U\Delta t}{\Delta x}$, where U is the characteristic flow velocity, Δt is the time step size, and Δx is the minimum grid spacing. For stable free-surface flow simulations, it is generally recommended to maintain Co within the range of 0.1–0.5. Therefore, the time-step refinement study presented here primarily aims to examine the temporal stability and accuracy of the wave propagation, rather than serving as a convergence study. The corresponding Courant numbers for cases T1–T4 are summarized in Table 2.

The Figures 11–13 below shows the temporal variations in free-surface elevations at three monitoring locations (3 m, 5 m, and 8 m downstream) under different time steps (T1–T4).

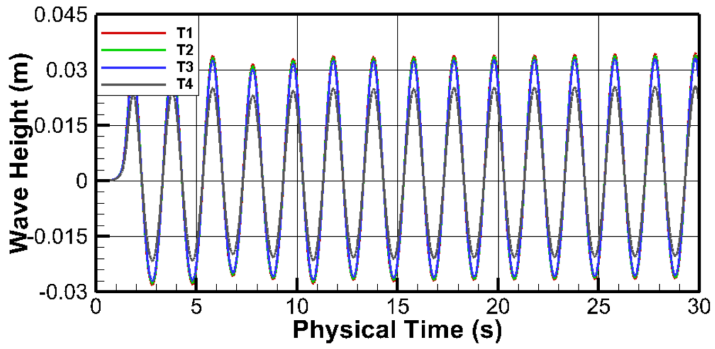


Figure 11. Wave elevation comparison at 3 m downstream (T1–T4).

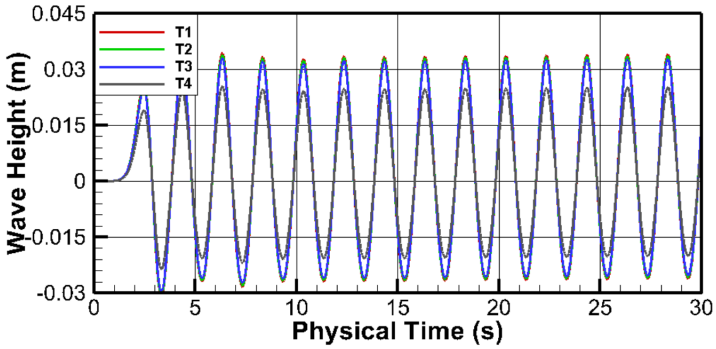


Figure 12. Wave elevation comparison at 5 m downstream (T1–T4).

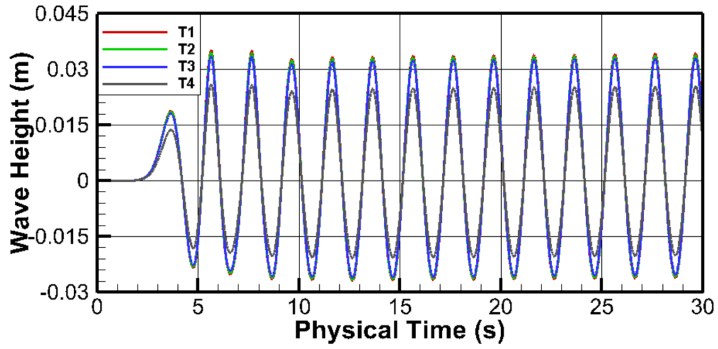


Figure 13. Wave elevation comparison at 8 m downstream (T1–T4).

The theoretical wave height in this study is 0.6 m. Figure 14 compares the numerically simulated wave heights with the theoretical predictions at a distance of 3 m from the wavemaker (X = 3 m). In Cases T2, T3, and T4, the simulated wave heights show excellent agreement with the theoretical results, achieving an overall accuracy exceeding 98%. In contrast, Case T1, which employs a larger time-step size corresponding to a non-dimensional ratio of $T/\Delta t = 400$, exhibits a significant decrease in accuracy, with the predicted wave height reaching only about 86% of the theoretical value. This indicates the presence of notable numerical damping effects under coarse temporal resolution.



Figure 14. Comparison of numerical and theoretical wave height accuracy under different time step sizes at X = 8 m.

Considering all cases, the configuration used in Case T2—with 600 times steps per wave period—achieves a favorable balance between numerical accuracy and stability, and is therefore adopted for all subsequent simulations.

3.3. Piston-Type Wave Maker

To accurately represent the paddle motion, an overset mesh was employed around the piston region. Interpolation between the background and overset regions was handled using STAR-CCM+'s built-in volume fraction interpolation scheme. No special near-wall treatment was required, as the clearance between the moving paddle and the tank boundaries was sufficient to avoid mesh overlap issues. The total number of grid cells in the simulation model was approximately 5.5×10^6.

For the free-surface capturing, the VOF method was adopted in conjunction with the HRIC (High-Resolution Interface Capturing) scheme to minimize numerical diffusion at the interface. A variable time step was used to maintain the global CFL number below 0.1 throughout the domain, ensuring stable and accurate wave propagation.

As shown in Figure 15, the same base grid size and extruder mesh configuration are employed to construct numerical wave tanks for five different water depths (H): 0.5 m, 1.0 m, 1.5 m, 2.0 m, and 2.5 m. Measurement points are strategically positioned at distances of 3 m, 5 m, and 8 m from the wave paddle. Waves with a period of 2 s and a target wave height of 0.06 m are generated, and the resulting wave profiles are compared against corresponding theoretical values to evaluate the accuracy of the simulation.

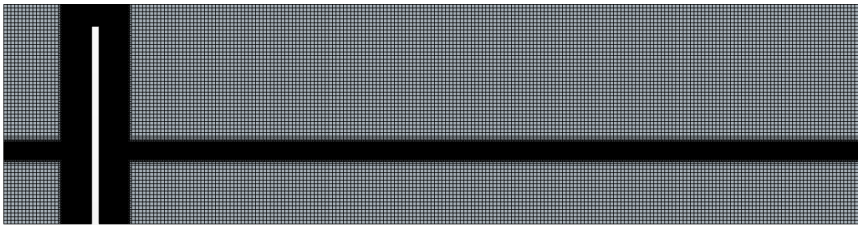


Figure 15. Local mesh refinement near the piston-type wavemaker region.

This figure illustrates the overall layout and zoning of the piston-type wavemaker mode in a numerical or physical wave tank. The wavemaker is installed on the left side and generates waves in the wave generation zone through periodic rotation about a hinge point. The generated waves propagate rightward through the working zone and are subsequently absorbed in the damping zone to minimize wave reflection. The still water depth is denoted by h, while the total tank length is represented by L. The region above the free surface corresponds to the air phase, and a wave probe is positioned within the working zone to record temporal variations in wave elevation.

In Figures 16–18, the performance of the piston-type wavemaker is evaluated in STAR-CCM+ at water depths of 0.5 m, 1.0 m, 1.5 m, 2.0 m, and 2.5 m. Wave height profiles are examined at measurement locations 3 m, 5 m, and 8 m downstream of the wavemaker.

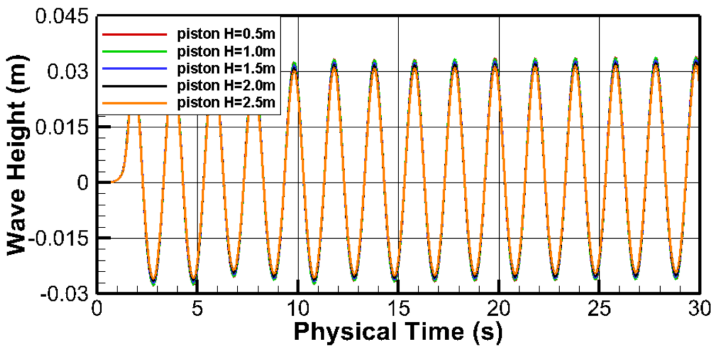


Figure 16. Wave height characteristics generated by a piston-type wave generator according to changes in water depth at X = 3 m.

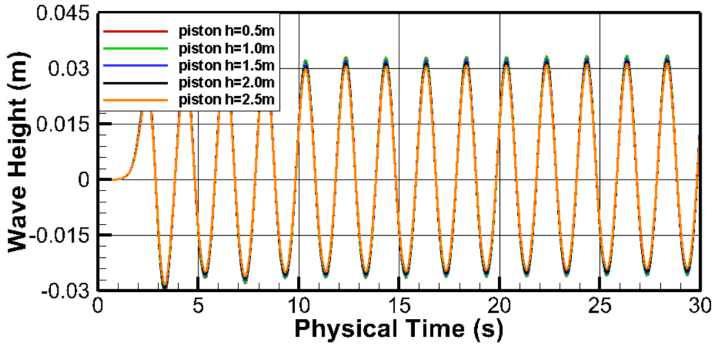


Figure 17. Wave height characteristics generated by a piston-type wave generator according to changes in water depth at X = 5 m.

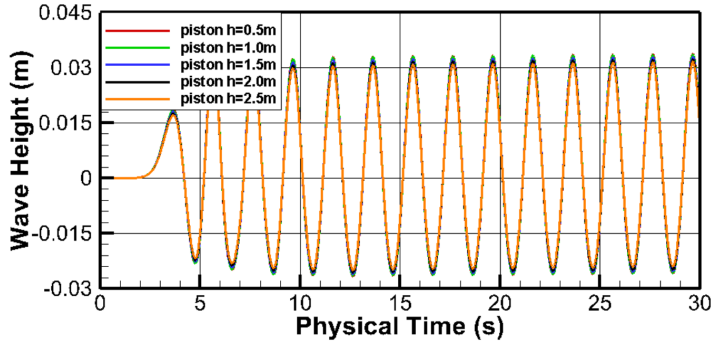


Figure 18. Wave height characteristics generated by a piston-type wave generator according to changes in water depth at X = 8 m.

3.4. Flap-Type Wave Maker

The numerical wave tank used for simulating flap-type wave generation is the same as that for the piston-type case in Figure 19. The base mesh size for both the wave paddle and the tank is 0.05 m, and the vertical resolution near the free surface is refined to 0.003 m. The grid density is further increased toward the tank bottom and the wave paddle, with a minimum cell height of 0.0015 m. Across the free surface, two mesh resolutions are employed—0.23 m (coarse) and 0.12 m (fine). An overset mesh is applied to the paddle region, yielding a total of 7.6×10^6 cells. The numerical wave tank is configured for five water depths: 0.5 m, 1.0 m, 1.5 m, 2.0 m, and 2.5 m. Measurement points are located 3 m, 5 m, and 8 m downstream of the wavemaker. A wave period of 2 s and a wave height of 0.05 m are prescribed.

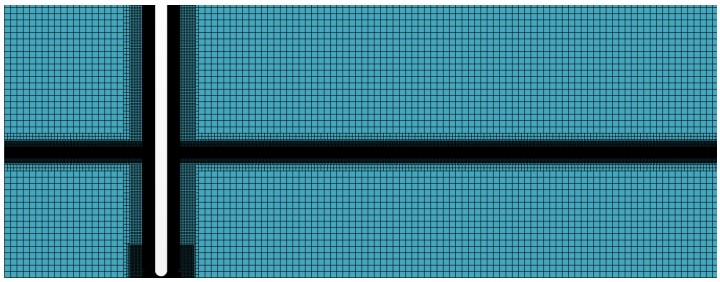


Figure 19. Local mesh refinement near the flap-type wavemaker region.

Figures 20–22 compare the wave height profiles generated by the flap-type wave maker at measurement locations X = 3 m, 5 m, and 8 m across various water depths (h = 0.5 m, 1.0 m, 1.5 m, 2.0 m, and 2.5 m). The results indicate that, at a given measurement point, the relative numerical error decreases as the water depth increases.

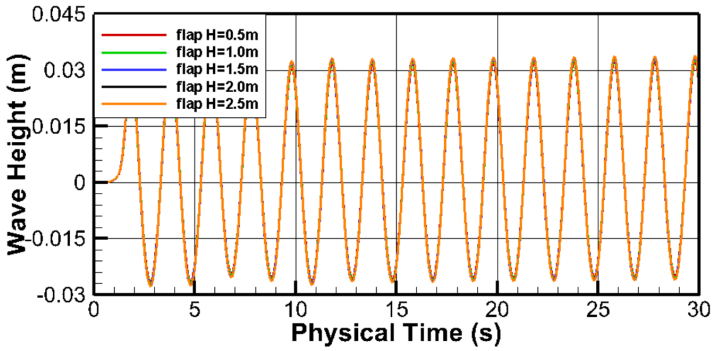


Figure 20. Wave height characteristics generated by a flap-type wave generator according to changes in water depth at X = 3 m.

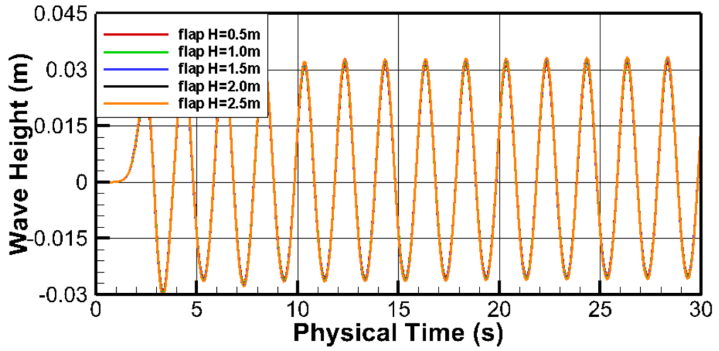


Figure 21. Wave height characteristics generated by a flap-type wave generator according to changes in water depth at X = 5 m.

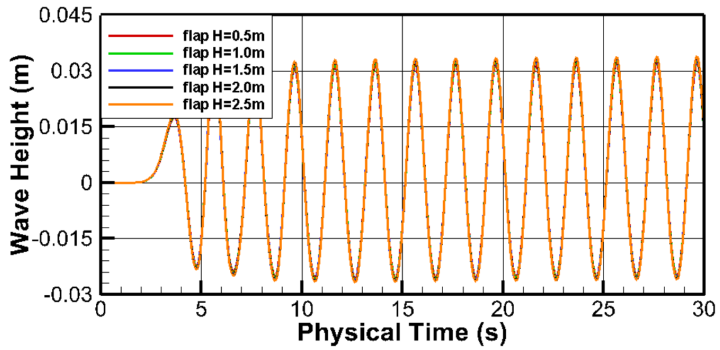


Figure 22. Wave height characteristics generated by a flap-type wave generator according to changes in water depth at X = 8 m.

3.5. Double-Flap Wave Maker

A numerical wave tank measuring 60 m (length) × 0.1 m (width) × 3 m (height) was constructed to simulate the performance of the double-flap wave maker. The wave maker consists of two independently controlled flaps. The computational domain from 20 m to 60 m was meshed using the extruder mesh function with 18 layers and a stretching factor of 25. The base mesh size for the wave paddles and tank walls was set to 0.05 m, while the mesh height near the free surface was refined to 0.003 m. The mesh resolution across the free surface was defined as 0.24 for the coarse configuration and 0.12 for the fine configuration. Additionally, to better capture flow behavior near the bottom boundary, the mesh density was gradually increased toward the tank floor, as illustrated in Figure 23. The total number of cells in the computational mesh amounted to 2,240,754.

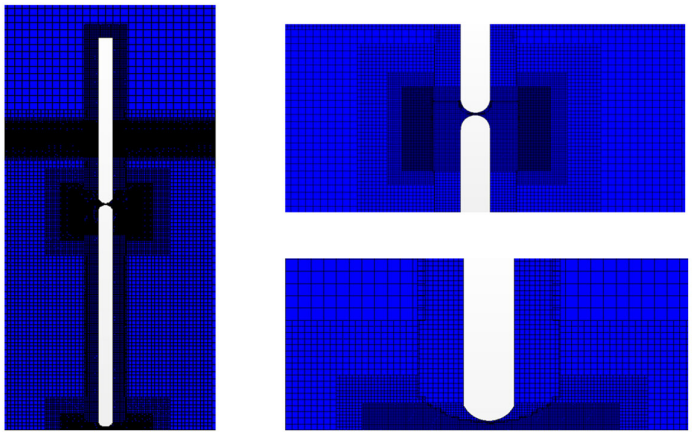


Figure 23. Local mesh refinement near the double flap-type wavemaker region.

Simulations were conducted using a wave period of 2 s and a target wave height of 0.06 m. Three water depths—1.0 m, 2.0 m, and 2.5 m—were considered to investigate the influence of depth on wave generation.

Figures 24–26 display the wave height profiles obtained from STAR-CCM+ simulations of the double-flap wave maker under varying water depths of 1.0 m, 2.0 m, and 2.5 m. The wave heights were recorded at measurement locations positioned at 3 m, 5 m, and 8 m along the x-direction. As the water depth increases, the simulated wave heights at each measurement point show improved stability and consistency, indicating enhanced accuracy of wave generation under deeper water conditions.

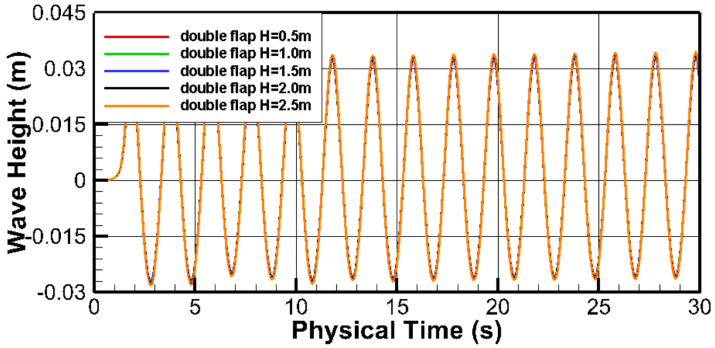


Figure 24. Wave height characteristics generated by a double-flap type wave generator according to changes in water depth at X = 3 m.

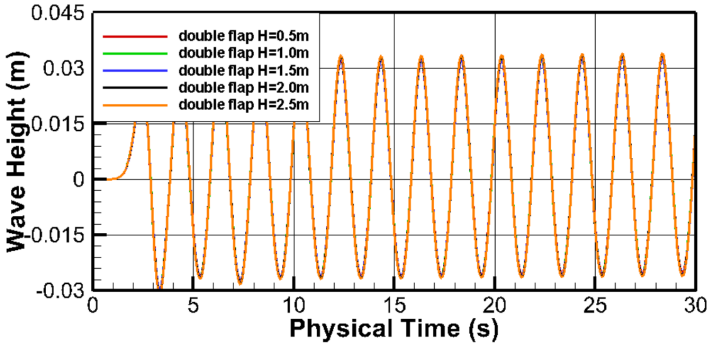


Figure 25. Wave height characteristics generated by a double-flap type wave generator according to changes in water depth at X = 5 m.

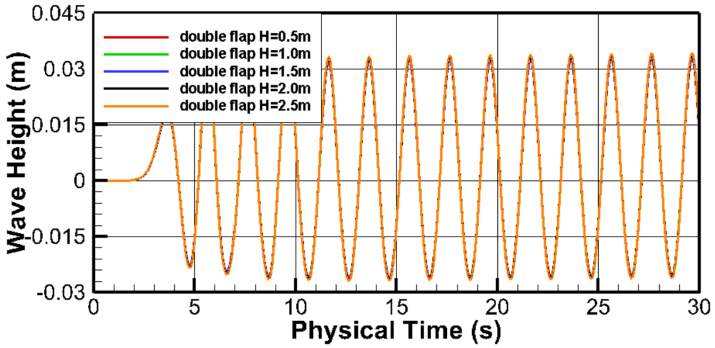


Figure 26. Wave height characteristics generated by a double-flap type wave generator according to changes in water depth at X = 8 m.

3.6. Comparison of Piston-Type, Flap-Type and Double Flap-Type Wave Makers

In the following figures, the blue line represents the theoretical wave solution for the piston-type wave maker, while the red line represents the theoretical solution for the flap-type wave maker. The points indicate the values of kh and H/S obtained for both types of wave makers at different water depths of 0.5 m, 1.0 m, 1.5 m, 2.0 m, and 2.5 m.

Figures 27–29 illustrate the variation in the non-dimensional wave height (H/S) with respect to the wave number–depth product (kh), comparing the numerical and theoretical results for both piston-type and flap-type wave makers. At measurement locations of 3 m and 5 m, the piston-type wave maker exhibits a greater deviation from the theoretical values than the flap-type. As shown in Figure 29, this trend continues at the 8 m location, where the piston-type wave maker demonstrates a noticeably larger error. Nevertheless, it is also evident that the numerical error for the flap-type wave maker increases with the distance from the wave paddle, indicating the influence of propagation distance on accuracy for both types.

The following wave profiles compare the wave heights generated by the piston-type, flap-type, and double-flap-type wavemakers at three different water depths (0.5 m, 1.0 m, 1.5 m, 2.0 m and 2.5 m). The results show noticeable differences in wave patterns and propagation stability between the three wavemaker types under shallow and deep-water conditions, providing a useful basis for subsequent performance analysis.

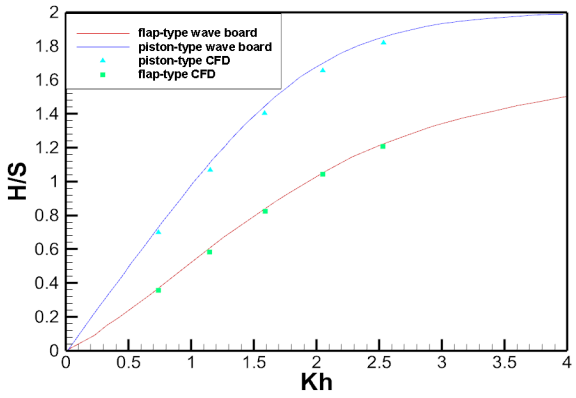


Figure 27. The comparison of theoretical result and CFD result for Piston and Flap type wavemaker at 3 m position from inlet.

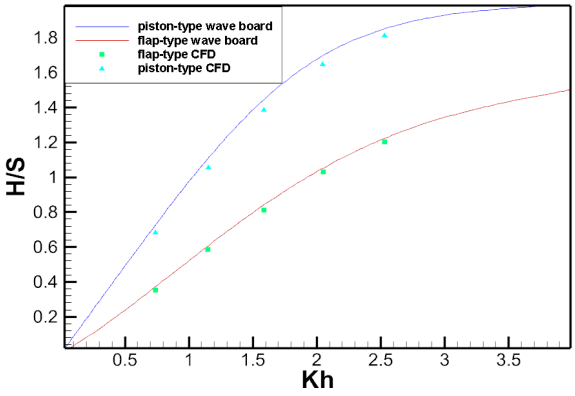


Figure 28. The comparison of theoretical result and CFD result for Piston and Flap type wave maker at 5 m position from inlet.

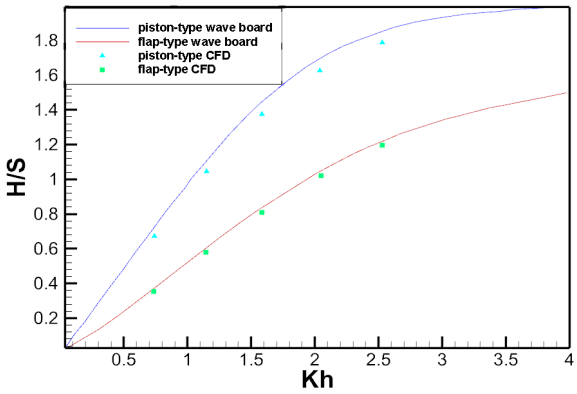


Figure 29. The comparison of theoretical result and CFD result for Piston and Flap type wave maker at 8 m position from inlet.

The comparative results presented in Figures 30–34 clearly demonstrate that the wave-generation performance of the piston-type, flap-type, and double-flap-type wavemakers varies significantly with water depth. At shallow-water conditions, particularly at a water depth of 0.5 m and 1.0 m, the piston-type wavemaker consistently produces the largest wave heights among the three configurations at all measurement locations (3 m, 5 m, and 8 m). Its translational motion is more compatible with shallow-water wave characteristics, enabling more efficient volumetric displacement and resulting in smaller deviations from the target wave height. This superior shallow-water performance is reflected by the closer alignment between the piston-type results and the intended wave amplitude.

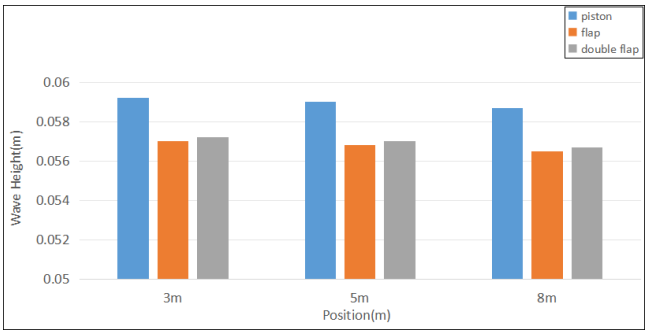


Figure 30. Comparison of wave heights produced by the piston, flap, and double-flap wavemakers at a water depth of 0.5 m.

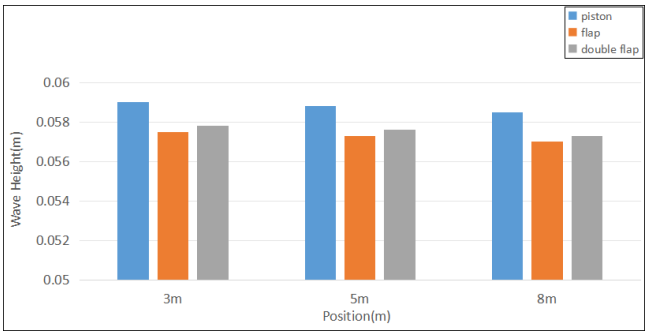


Figure 31. Comparison of wave heights produced by the piston, flap, and double-flap wavemakers at a water depth of 1.0 m.

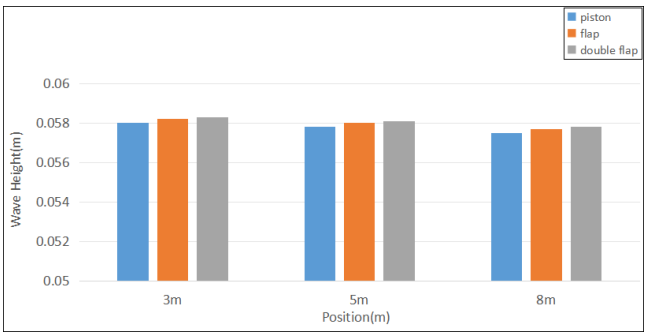


Figure 32. Comparison of wave heights produced by the piston, flap, and double-flap wavemakers at a water depth of 1.5 m.

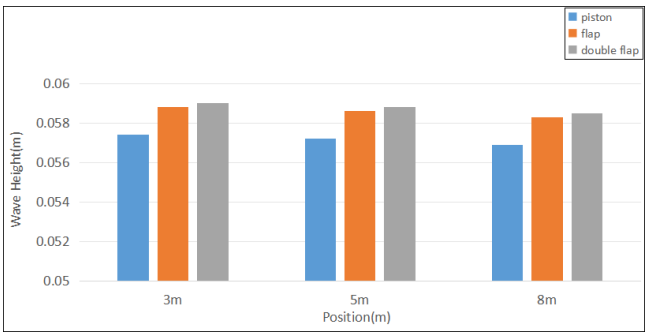


Figure 33. Comparison of wave heights produced by the piston, flap, and double-flap wavemakers at a water depth of 2.0 m.

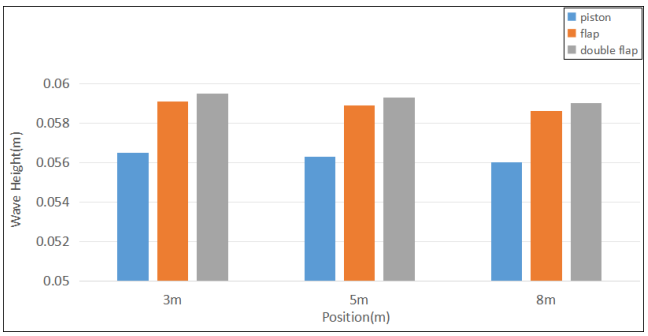


Figure 34. Comparison of wave heights produced by the piston, flap, and double-flap wavemakers at a water depth of 2.5 m.

However, as the water depth increases to 1.5 m, 2.0 m, and 2.5 m, the flap-type and double-flap-type wavemakers exhibit increasingly better performance. In deeper water, the

piston-type wavemaker shows noticeable attenuation with distance, while both the flap and double-flap configurations maintain more stable wave heights along the propagation path. This improvement arises from the rotational motion of flap-based wavemakers, which generates free-surface profiles and velocity distributions more consistent with deep-water wave theory. Among them, the double-flap wavemaker demonstrates the highest consistency, producing nearly uniform wave heights across different depths and measurement positions, indicating superior control over wave formation.

4. Conclusions

This study performed a numerical investigation of the wave generation performance of piston-type, flap-type, and double-flap-type wave makers using the STAR-CCM+ platform. The investigation focused on assessing wave height accuracy under varying water depths and measurement locations. The present results exhibit good agreement with previous experimental and numerical studies [19,24], confirming the reliability and validity of the adopted numerical approach for piston-, flap-, and double-flap-type wavemakers in two-dimensional CFD wave tanks.

The results indicate that the error associated with the piston-type wavemaker increases with water depth, although it still maintains reasonably good numerical stability and accuracy under deep-water conditions. Overall, the simulated wave heights produced by all three wavemaker types converge toward the theoretical values as the water depth increases. However, the piston-type wavemaker exhibits the largest deviations, particularly near the wave paddle. For example, at a water depth of 1.0 m and a measurement location 8 m downstream, the piston-type configuration produces a wave-height error of 5.6%, compared with 4.7% for the flap-type. In addition, the piston-type wavemaker shows more pronounced wave-amplitude attenuation with propagation distance, suggesting greater energy dissipation associated with its translational motion during long-distance propagation.

The double-flap-type wavemaker exhibited a consistent ability to reproduce wave heights that closely matched theoretical predictions, particularly under deeper-water conditions such as 2.0 m and 2.5 m, where the errors generally remained below 3%. This superior performance can be attributed to its dual-segment configuration, which provides greater flexibility in paddle motion compared with single-plate mechanisms, thereby enabling more precise control over wave formation. However, these findings are subject to certain limitations. The present analysis was conducted within a two-dimensional VOF-based CFD framework using the RNG k-ω turbulence model and was restricted to a specific range of water depths. Moreover, only near-field measurement locations ($\leq$8 m) were considered, meaning that far-field wave transformation, reflection characteristics, and the potential onset of Benjamin–Feir instability were not evaluated.

Overall, the results indicate that the double-flap configuration holds considerable promise for high-fidelity wave generation in both numerical and experimental applications. Future research will extend the propagation distance and incorporate long-term wave evolution to better assess wave-quality retention over larger spatial domains. Additional efforts will focus on nonlinear and three-dimensional simulations, systematic investigation of inter-flap phase control, and comprehensive validation against laboratory experiments. These developments will help improve the robustness, reliability, and broader applicability of the comparative conclusions drawn in this study.

Author Contributions: Conceptualization, K.Y.; Methodology, K.Y.; Data curation, K.Y. and H.D.; Writing—original draft preparation, H.D.; Review and editing, J.O. and D.S. All authors have read and agreed to the published version of the manuscript.

Funding: This research was supported by a grant (RS-2025-07282968) of Cooperative Research Method and Safety Management Technology in National Disaster funded by Ministry of Interior and Safety (MOIS, Republic of Korea).

Data Availability Statement: The original contributions presented in this study are included in the article. Further inquiries can be directed to the corresponding author.

Conflicts of Interest: The authors declare no conflicts of interest.

References

1. Dean, R.G.; Dalrymple, R.A. *Water Wave Mechanics for Engineers and Scientists*; World Scientific: Singapore, Singapore, 1991.
2. Blenkinsopp, C.E.; Chaplin, J.R. The effect of relative crest submergence on wave breaking over submerged slopes. *Coast. Eng.* **2008**, *55*, 967–974. [CrossRef]
3. Kim, H.; Oh, J.; Lew, J.-M.; Rhee, S.H.; Kim, J.H. Wave and wave board motion of hybrid wave maker. *J. Soc. Nav. Archit. Korea* **2021**, *58*, 339–347.
4. Kwon, J.; Oh, J.; Kim, H.; Lew, J.-M. Linear analysis of water surface waves generated by submerged wave board whose upper and lower ends oscillate horizontally freely. *J. Soc. Nav. Archit. Korea* **2019**, *56*, 418–426.
5. Oh, J.; Kim, J.-Y.; Kim, H.; Kwon, J.; Lew, J.-M. Approximate solution of vertical wave board oscillating in submerged condition and its design application. *J. Soc. Nav. Archit. Korea* **2018**, *55*, 527–534. [CrossRef]
6. Binh, P.C.; Hai, N.L.D. A study on design and fabrication of a wave maker in laboratory environment. In Proceedings of the 2023 8th International Scientific Conference on Applying New Technology in Green Buildings (ATiGB), Danang, Vietnam, 10–11 November 2023; ISBN 979-8-3503-4397.
7. Fouques, S.; Laflèche, S.; Akselsen, A.; Sauder, T. An experimental investigation of nonlinear wave generation by flap wavemakers. In *International Conference on Ocean, Offshore and Arctic Engineering, Proceedings of the ASME 2021 40th, Virtual Conference, 21–30 June 2021*; The American Society of Mechanical Engineers (ASME): Houston, TX, USA, 2021; Paper No. OMAE2021-63120.
8. Shehab, A.; El-Baz, A.M.R.; Elmarhomy, A.M. CFD modeling of regular and irregular waves generated by flap-type wave maker. *J. Adv. Res. Fluid Mech. Therm. Sci.* **2021**, *85*, 128–144.
9. Lal, A.; Elangovan, M. CFD simulation and validation of flap-type wave-maker. *Int. J. Math. Comput. Sci.* **2008**, *2*, 10–16.
10. Nouioui, B.; Doğan, M. Irregular wavemaker (piston type) in a numerical and physical wave tank. *Usak Univ. J. Eng. Sci.* **2022**, *52*, 95–116. [CrossRef]
11. Krvavica, N.; Ružić, I.; Ožanić, N. New approach to flap-type wavemaker equation with wave breaking limit. *Coast. Eng. J.* **2018**, *60*, 69–78. [CrossRef]
12. Kusumawinahyu, W.M.; Karjanto, N.; Klopman, G. Linear theory for single and double flap wavemakers. *J. Indones. Math. Soc.* **2006**, *12*, 41–57.
13. Marques Machado Fábio, M.; Gameiro Lopes António, M.; Ferreira, A.D. Numerical simulation of regular waves: Optimization of a numerical wave tank. *Ocean. Eng.* **2018**, *170*, 89–99.
14. Folley, M.; Whittaker, T.J.T.; Henry, A. The effect of water depth on the performance of a small surging wave energy converter. *Ocean. Eng.* **2007**, *34*, 1265–1274. [CrossRef]
15. Tian, X.; Wang, Q.; Liu, G.; Deng, W.; Gao, Z. *Numerical and Experimental Studies on a Three-Dimensional Numerical Wave Tank*; IEEE Access: New York, NY, USA, 2018; Volume 6, p. 99.
16. An, S.-H.; Lee, J.-H. Analysis of overtopping wave energy converters with ramp angle variations using particle-based simulation. *J. Adv. Mar. Eng. Technol.* **2024**, *48*, 414–420. [CrossRef]
17. An, S.-H.; Lee, J.-H. Effects of wave generation distance in particle-based numerical wave tank on the analysis of overtopping wave energy converters. *J. Adv. Mar. Eng. Technol.* **2024**, *48*, 459–465. [CrossRef]
18. Ramezanzadeh, S.; Ozbulut, M.; Yildiz, M. Simulation of irregular wave motion using a flap-type wavemaker. In Proceedings of the VIII. International Conference on Computational Methods in Marine Engineering (MARINE 2019), Gothenburg, Sweden, 13–15 May 2019.
19. Elangovan, M.; Lal, A. Simulation and validation of plunger type wave maker by CFD. *ResearchGate*. 2010. Available online: https://www.researchgate.net/publication/290952269 (accessed on 11 October 2025).
20. Wang, Q.; Li, M. Wave generation by flap-type wavemaker in circular arc numerical wave tanks. *IOP Conf. Ser. Earth Environ. Sci.* **2018**, *170*, 022021. [CrossRef]
21. Liu, Y.; Zheng, Y.; Song, R.; Chen, J.; Jin, H. Wave generation characteristic analysis of piston and flap-type wave maker with rotary-valve-control vibrator. *J. Vib. Control* **2022**, *26*, 15–16. [CrossRef]
22. Park, J.; Cho, D.; Jang, T. A numerical experiment on a new piston-type wavemaker: Shallow water approximation. *Int. J. Nav. Archit. Ocean Eng.* **2023**, *15*, 100053. [CrossRef]

23. Kim, S.Y.; Kim, K.M.; Park, J.C.; Jeon, G.-M.; Chun, H.-H. Numerical simulation of wave and curent interaction with a fixed offshore substructure. *Int. J. Nav. Archit. Ocean Eng.* **2016**, *8*, 188–197. [CrossRef]
24. Hyun, J.M. Theory for Articulated Double-Flap Wavemakers in Water of Constant Depth. *J. Soc. Nav. Archit. Jpn.* **1977**, *141*, 78–85. [CrossRef]
25. Hughes, S.A. *Physical Models and Laboratory Techniques in Coastal Engineering*; World Scientific: Singapore, Singapore, 1993; Chapter 7.
26. Madsen, O. Waves generated by a piston-type wavemaker. *Coast. Eng.* **1970**, *1*, 36. [CrossRef]
27. Issa, R.I. Solution of the implicitly discretised fluid flow equations by operator-splitting. *J. Comput. Phys.* **1986**, *62*, 40–65. [CrossRef]
28. Ferziger, J.H.; Perić, M. *Computational Methods for Fluid Dynamics*; Springer: Berlin/Heidelberg, Germany, 2002.

Disclaimer/Publisher's Note: The statements, opinions and data contained in all publications are solely those of the individual author(s) and contributor(s) and not of MDPI and/or the editor(s). MDPI and/or the editor(s) disclaim responsibility for any injury to people or property resulting from any ideas, methods, instructions or products referred to in the content.